CrystEngComm

Accepted Manuscript

ROYAL SOCIETY OF CHEMISTRY

www.rsc.org/crystengcomm

Journal Name

RSCPublishing

ARTICLE

Black Strontium Titanate Nanocrystals of Enhanced Solar Absorption for Photocatalysis

Cite this: DOI: 10.1039/xoxxoooooox

Wenli Zhao,[a] Wei Zhao,[a] Guilian Zhu,[a] Tianquan Lin,[a] Fangfang Xu*[a] and Fuqiang Huang*[a,b]

Received ooth January 2012,
Accepted ooth January 2012

DOI: 10.1039/xoxxoooooox

www.rsc.org/

Black titania have attracted enormous attention due to enhanced photocatalytic activity via increased solar absorption, but few studies extended the investigations to other wide band-gap titanates. Herein, strontium titanate $SrTiO_3$, a typical ternary titanate with more potential in photocatalysis, is selected as the target material. Black $SrTiO_3$ nanocrystals were obtained by molten aluminum reduction of solution-processed pristine $SrTiO_3$ in a two-zone furnace. Different from the black titania, black $SrTiO_3$ nanocrystals are well-crystallized and have no core-shell structure. Substantial Ti^{3+} cations and oxygen vacancies are introduced into $SrTiO_3$ after aluminum reduction, which results in the enhanced absorption in both visible and near-infrared regions and the improved charge separation and transport. The photocatalytic hydrogen-generation and photoelectrochemical investigations demonstrate that black $SrTiO_3$ exhibits impressively improvement (2.5 times and 2.4 times at 1.23 VRHE, respectively) compared with white $SrTiO_3$.

Introduction

Semiconductor photocatalysis offers an environmentally friendly approach for environmental protection and hydrogen energy generation with the assistance of solar light, and thus, it is considered to be a potential solution for tackling the energy shortage and counteracting environmental degradation.[1,2] Titanium dioxide (TiO_2), one of the most important semiconductor, has attracted intense exploration for its photocatalytic properties. However, its large band gap (~ 3.2 eV) captures only about 5% of solar energy, resulting in poor solar-to-hydrogen conversion efficiency.[3-5] Great efforts have been devoted to increasing visible-light absorption by band structure engineering (e.g. element doping or self-doping by oxygen deficiency).[3,6-8]

Recently, enhanced light absorption and photocatalytic activity were achieved in black titania via high H_2-pressure process or hydrogen gas annealing due to the additional intermediate electronic states induced by hydrogen insertion into the lattice of TiO_2.[9-13, 31-34,]. Hydrogen plasma treatment was also demonstrated to be an effective method to obtain H-doped black titania with efficient light absorption and high electron concentration.[14] In our previous study, molten aluminum was applied to prepare black titania with a unique core/shell structure instead of using hydrogen as the reducing agent.[15-18] The aluminum reduction is very efficient with manipulating oxygen partial pressure to obtain black titania at a moderate temperature (350 – 550 °C), which exhibited high solar absorption (65% of the total solar spectrum) and excellent photocatalysis.[16]

Similar to TiO_2, $SrTiO_3$ has a valence orbital (Ti 3*d*, O 2*p*) near Fermi surface but supplies a higher potential in facilitating the formation of hydrogen. In addition, $SrTiO_3$ has superior physical and chemical properties, such as the chemical and structural stability, great heat resistance, corrosion resistance and easy to modified by other substances. These merits make it become one of the promising photocatalytic candidates for TiO_2.[19-21] Unfortunately, $SrTiO_3$ also suffers from a wide band gap (~ 3.2 eV) and ineffective light absorption, especially in the visible and infrared light range, which largely restricts its practical applications in photocatalysis. Despite the thorough study of black titania, few studies extended to producing $SrTiO_3$ with effective light absorption. [35, 36] Thus, it is necessary to seek an effective method to promote $SrTiO_3$ with wide-spectrum response and high photocatalytic activity.

In this work, $SrTiO_3$ (STO), synthesized by alkaline hydrothermal method, is selected as the target material and subsequently reduced by aluminum in a two-zone tube furnace to prepare reduced $SrTiO_3$ (R-STO). The introduction of Ti^{3+} $3d^1$ states and oxygen vacancies into the lattice of $SrTiO_3$ causes impurity/defect states (oxygen vacancies) in the band gap, resulting in an enhancement in visible and infrared light absorption. Structural openness is increased due to the introduced defects, which benefits photocatalysis according to our previously proposed model of packing factor.[28, 29] The R-STO is demonstrated to exhibit a drastically enhanced photocatalytic hydrogen-generation and photoelectrochemical properties compared with the pristine STO.

Results and discussion

Fig. 1 shows the absorption spectra of STO and R-STO nanoparticles. Compared with the pristine STO, R-STO extends the photoresponse from UV light to visible and infrared light regions. In good agreement with these measurements, as-prepared STO is white in color and R-STO is black, as shown in the inset of Fig. 1. The absorption edges of STO and R-STO both locate at 386 nm, which corresponds to the bandgap of 3.2 eV. The pristine and reduced $SrTiO_3$ prepared by solid-state reaction, which was denoted as SSR-STO and R-SSR-STO (see in experimental section), are also conducted absorption spectra test, as show in Fig. S1. Similarly, the R-SSR-STO is also black in color, exhibiting significant enhancement in visible and near-infrared photo absorption. In brief, aluminum reduction can effectively enhance the absorption of $SrTiO_3$ in the visible and near infrared light region.

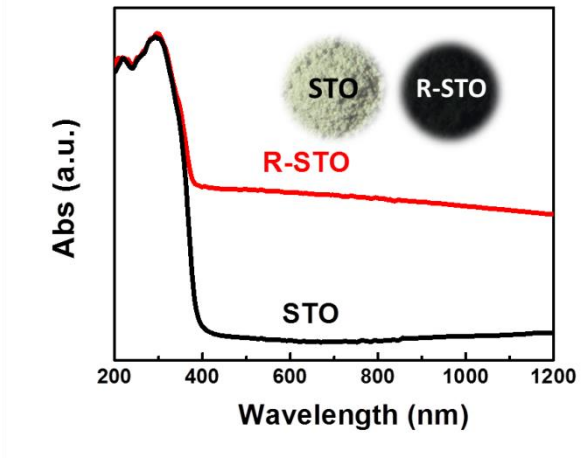

Figure 1. Diffuse reflectance spectra of STO and R-STO samples.

The X-ray diffraction (XRD) patterns (Fig. 2a) indicated that the STO is centrosymmetry cubic perovsike structure $SrTiO_3$ with space group P*m-3m* (JCPDS Card: 78-2486) and a small amount of anatase generated during the synthesis procedure. No phase transition is observed after Al reduction treatment, both the $SrTiO_3$ and anatase phase maintain.

Raman spectroscopy is very sensitive to short-range distortions arising from microstructural defects. The Raman spectra of STO and R-STO collected at room temperature are depicted in Fig. 2b. $SrTiO_3$ has centrosymmetric cubic perovskite structure with space group P*m-3m*, so the room temperature spectra should be dominated by second-order scattering.[22,23] It can be found that both STO and R-STO include two broad bands centered in the 200–500 and 600–800 cm^{-1} regions, which agree well with the previous studies. [22] It means R-STO still maintains the basic structural and lattice dynamical properties of STO. Four additional peaks at ~ 174 cm^{-1}, 541 cm^{-1}, 682 cm^{-1} and 791 cm^{-1} in STO belong to the first-order scattering and show an excellent match with the frequencies of TO2, TO4, TO and LO4 phonons, respectively.[23] After aluminum reduction, the intensity of both the two broad bands declined, which may suggest a weaker centrosymmetry of R-STO sample. Additionally, it is worthwhile to note that R-STO shows a blue shift and a broadening line width of the Raman peak at 174 cm^{-1}, which can be attributed to the introduced oxygen vacancies. TO4 mode, indicating optical modes of high longitudinal frequency with A1 symmetry for the [TiO6] octahedron, decays after Al-reduction process and may be associated with the presence of oxygen vacancies as well. [23]

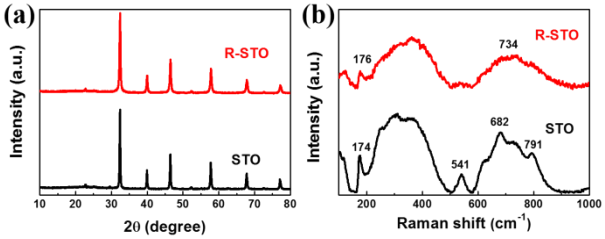

Figure 2. (a) XRD patterns and (b) Raman spectra of STO and R-STO samples.

Given the fact that molten aluminum can decrease the oxygen partial pressure to form a reducing environment by forming aluminum oxide according to the Ellingham diagram,[16] annealing in a reductive environment creates a certain number of oxygen vacancies in the $SrTiO_3$ crystal structure. The newly formed oxygen vacancies of reduced samples facilitate lattice rearrangement and increase the structural openness. Based on our previous model for the structure–property relationship of photocatalytic materials, higher structural openness degree, in accordance with lower packing factor, is associated with stronger ability for electron–hole separation and transfer, and usually results in better photocatalytic activity.[27,28] Therefore, the photocatalytic activity of R-STO would be superior to STO.

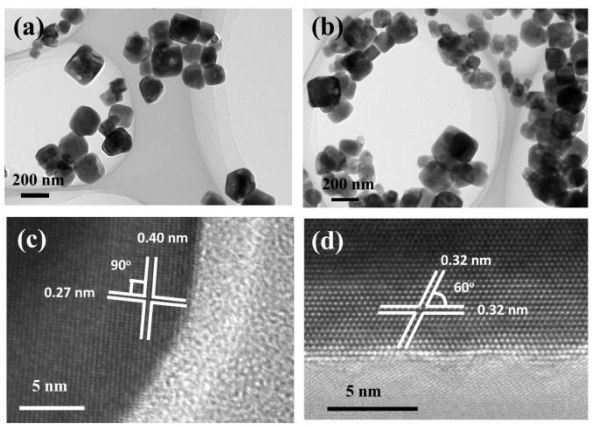

Figure 3. TEM image of STO (a) and R-STO (b). High resulution TEM image of STO (c) and R-STO nanocrystal (d).

The morphology of the R-STO was investigated by scanning electron microscopy (SEM) as shown in Fig. S2a. It is indicated that the R-STO nanocrystals are 100 – 200 nm in diameter. The TEM images show a similar morphology and particle size of STO (Fig. 3a) and R-STO (Fig. 3b), which proves Al reduction treatment do not

change the morphology of samples. A typical high-resolution transmission electron microscopy (HRTEM) image (Fig. 3c) of STO shows two sets of lattice fringes with spacing of 0.27 and 0.40 nm, corresponding to {110} and {001} atomic planes of the $SrTiO_3$, respectively. HRTEM image of R-STO is presented in Fig. 3d. Well-resolved {110} lattice planes of R-STO with plane distances of 0.32 nm is observed, and the measured intersection angle between the two planes agrees well with the calculated value of 60°. Selected-area electron diffraction (SAED) pattern (Fig. S2b) for the corresponding single R-STO nanoparticle demonstrates that nanoparticles are single crystalline and well-crystallized with atomic planes. These TEM results, in combination with the above XRD and Raman analysis, definitely demonstrate that the synthesized powder is pure anatase and keeps phase stabilization during aluminum reduction. However, both of R-STO and STO are highly crystallized as its lattice fringes extending to the particle margins clearly instead of a specific core/shell structure consisting of a disordered surface layer and a crystalline core which is commonly noticed in the case of black TiO_2.[16,17]

In the case of hydrogenated anatase TiO_2, the enhanced light absorption is attributed to hydrogenation-generated surface disorder of TiO_2 and the resulted localized surface plasma resonance.[14] In our black R-STO, aluminum reduction does not induce obvious surface disorder (Fig. 3d), but according to the above analysis of XRD and raman spectroscopy of STO and R-STO (Fig. 2a and 2b), it reinforces the structural openness and introduces Ti^{3+} and oxygen vacancies in R-STO, which may contribute to charge transfer and inhibit charge recombination. These aspects might work together to lead to the enhanced light absorption and black coloration of R-STO. Besides, for black titania, the introduced metastable sites (surfaced Ti^{3+} ions, oxygen vacancies) is easily transported to the loosely packed amorphous shells and oxidized by certain components (O_2, H_2O, etc.) during photocatalytic reaction, which can be proved by their decreased photocatalytic performance in cycling tests.[16,17] In black R-STO, however, due to its well crystallization and absence of amorphous layer, newly-formed Ti^{3+} cations and oxygen vacancies are relatively stable, which can be expected to be more outstanding in photocatalytic stability.

The photoluminescence emission spectra (PL) is effective in tracking the behavior of light-excited electrons and holes in semiconductors since PL emission results from the recombination of free charge carriers. The PL spectra of $SrTiO_3$ samples in the wavelength range of 400 – 800 nm with the excitation at 320 nm are shown in Fig. 4a. The intensities of PL peaks of the black R-STO reveal a significant decrease compared with STO, which indicates that the recombination rate of photogenerated electrons and holes is suppressed in R-STO. Given the fact that oxygen vacancies (V_O) usually serve as electron traps, thus the weaker intensity should be owing to the increased oxygen vacancies in R-STO, which inhibits charge recombination and favors high photocatalytic activity.

In order to further confirm the existence of Ti^{3+} and oxygen vacancies and illustrate the effect of aluminum reduction on improving the photoactivity in both the UV and visible regions, X-ray photoelectron spectroscopy (XPS) is employed to investigate the transformation of surface chemical bonding and detect the electronic valence band position of STO and R- STO. As shown in Fig 4b, the Ti 2*p* XPS spectrum of STO shows the typical pattern of Ti^{4+}-O bonds in $SrTiO_3$ with Ti $2p_{3/2}$ and $2p_{1/2}$

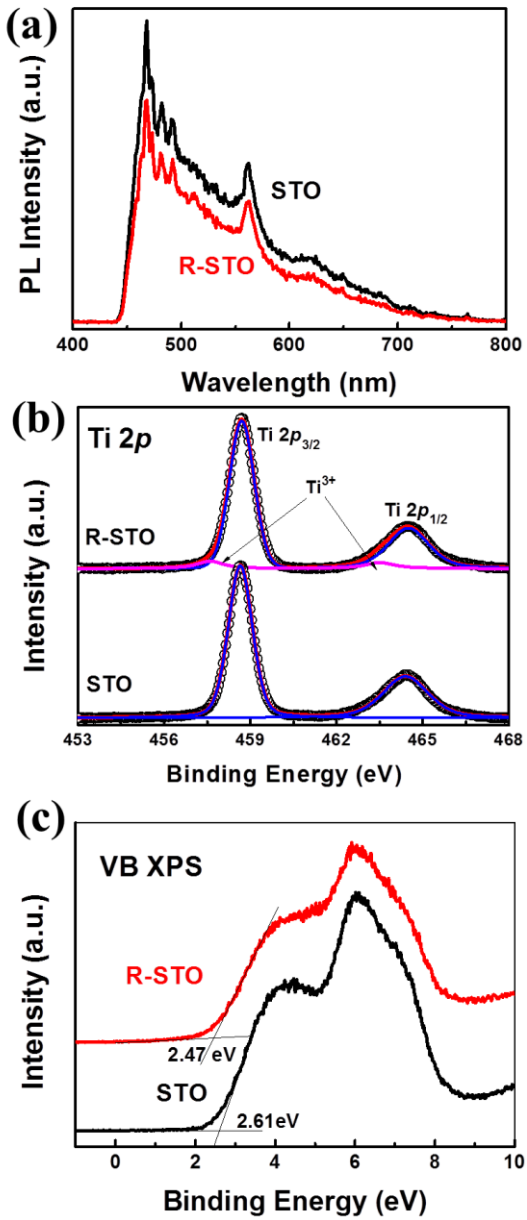

Figure 4. (a) Photoluminesent spectra; (b) Ti 2*p* XPS spectra of STO and R-STO. The black circles are the experimental data, which can be decomposed into a superposition of two fitting curves of Ti^{4+} (shown in blue) and Ti^{3+} (shown in pink). The red curve is the summation of the two decomposed curves. (c) valence-band XPS spectra of STO and R-STO samples.

peaks centered at binding energies of 458.6 eV and 464.4 eV.[3] Compared with the STO, additional small peaks centering separately at 457.6 eV and 463.5 eV in the R-STO conform to the $2p_{3/2}$ and $2p_{1/2}$ peaks of Ti^{3+}.[30] The emerging Ti^{3+} signals suggest that oxygen vacancies are introduced into the R-STO during the Al reduction process, which is consistent with the

Raman analysis. The generated Ti^{3+} cations and oxygen vacancies in the R-STO can serve as donors to increase the electron concentration of anatase TiO_2.

The XPS valence band (VB) spectra of STO and R-STO nanocrystals are showed in Fig. 4c. The valence band maxima are estimated by linear extrapolation of the peaks to the baselines.[26] The valence band maximum position shifts slightly from 2.61 eV of STO to 2.47 eV of R-STO below the Fermi energy, which may be due to that the disorders and defects induced by Al reduction generate some localized states above the valence band edge. Given the blue shift of the valence maximum, a narrowed band-gap would occur in the R-STO. However, the change of the band-gap is insufficient to exhibit in such an overall absorption in the visible and near infrared range. Besides, the band gap narrowing for R-STO due to the Ti^{3+} acceptor states can hardly be measured. Based on a previous report, a tail of conduction band about 0.7 eV below the conduction band maximum of TiO_2 could be generated. [16] The dark color of the R-STO could be derived from the formation of impurity/defect states (oxygen vacancies) in the band gap of R-STO during Al reduction treatment.

Clear ferromagnetic hysteresis loops for STO and R-STO are recorded at 2K (Fig. S3). The saturation magnetization *M*s is 0.020 emu g^{-1} for STO and 0.0570 emu g^{-1} for R-STO. The stronger magnetization may be partially correlated with the higher concentration of Ti^{3+} in R-STO.[16]

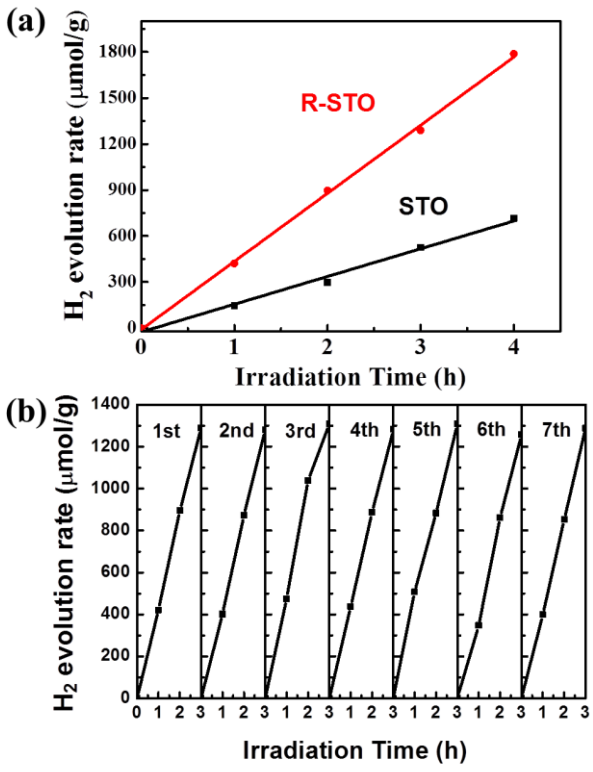

Figure 5. (a) solar-light driven photocatalytic water splitting for H_2 generation over STO and R-STO samples. (b) cycling tests of solar-driven photocatalytic activity of R-STO sample.

The photocatalytic activities of the STO and R-STO samples are evaluated by photocatalytic water splitting to produce hydrogen gas, as shown in Fig. 5a. R-STO sample steadily produce hydrogen gas at a rate of 444.2 μmol $h^{-1}g^{-1}$, which is 2.5 times higher than that of STO (181.0 μmol $h^{-1}g^{-1}$) and comparable to the reported excellent photocatalyst. Cycling tests reveal that the R-STO retains good photocatalytic activity in the first three photocatalytic cycles, as shown in Fig. 5b. The rate of H_2 evolution finally stabilized at about 430 μmol $h^{-1}g^{-1}$. As a comparison, the pristine and reduced $SrTiO_3$ prepared by solid-state reaction, which was denoted as SSR-STO and R-SSR-STO (see in experimental section), are also conducted photocatalytic hydrogen generation at the exactly same experimental conditions, and the rate of H_2 evolution are at 27.4 μmol $h^{-1}g^{-1}$ and 64.3 μmol $h^{-1}g^{-1}$ respectively (Fig. S4). Although the performance of SSR-STO and R-SSR-STO is virtually weaker than that of STO and R-STO duo to the larger particle size from solid-state reaction, the photocatalytic activity of SSR-STO is apparently improved after reduction treatment as well. These results have verified that the R-STO nanocrystals possess greatly promoted the photocatalytic activity.

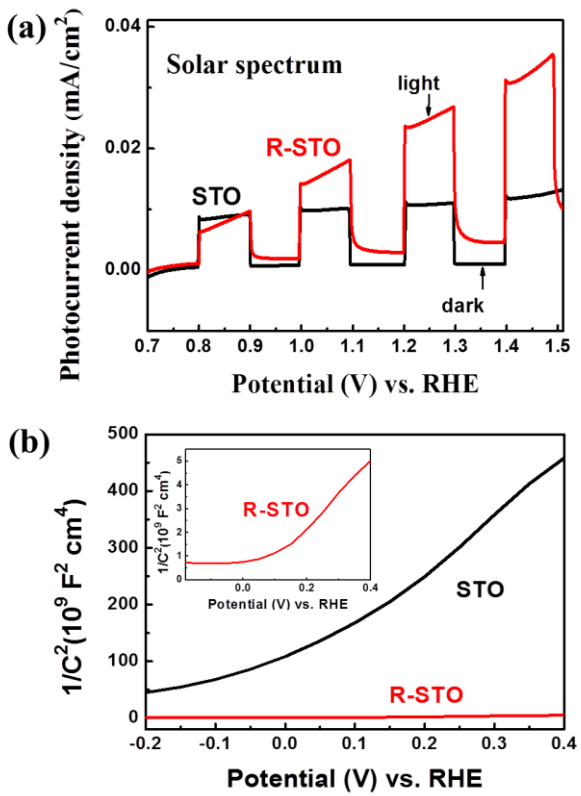

Figure 6. (a) Linear sweep voltammograms collected under 100 mW cm^{-2} illumination using a three electrode setup ($SrTiO_3$ working, Pt counter, Ag/AgCl reference electrode, scan rate of 20 mV s^{-1}) in a 1 M NaOH electrolyte (pH = 13.6). (b) Mott–Schottky plots collected at a frequency of 5 kHz in the dark.

In order to further investigate the photoelectrochemical properties, STO and R-STO films are prepared on FTO glass

substrates by dip-coating method. A set of linear sweeps were recorded in the dark and under 100 mW cm^{-2} illumination, as shown in Fig. 6a. The potential is swept linearly at a scan rate of 20 mV s^{-1} between 0.7 and 1.5 V_{RHE} in a 1 M NaOH electrolyte (pH= 13.6). Both photo electrodes show insignificant dark current, indicating that no electrocatalytic oxygen evolution occurs. Under illumination, the R-STO electrode has a significant increase in photocurrent density, which is about 2.4 times larger than that of STO at 1.23 V_{RHE} (corresponding to the potential of the reversible oxygen electrode). The higher photocurrent density demonstrates enhanced solar light absorption and more efficient charge separation and transportation in the black R-STO film, which is mainly caused by the increased amount of Ti^{3+} and oxygen vacancies.

In order to evaluate the carrier density of STO and R-STO to confirm the results above, the electrochemical impedance measurements are conducted on the STO and R-STO films. Both samples show a positive slope in the Mott–Schottky plots, which is typical for n-type semiconductors (Fig. 6b). Compared with STO film, the black R-STO film shows a substantially smaller slope of the Mott–Schottky plot, suggesting an increase of free charge carrier density. The carrier density can be calculated from the slope of Mott–Schottky plots by using the following equation,[27]

$$N_d = (2/e_0\varepsilon\varepsilon_0)[d(1/C^2)/dV]^{-1}$$

where e_0 is the electron charge, ε is the dielectric constant of $SrTiO_3$(ε =300), ε_0 is the permittivity of vacuum, N_d is the donor density, and V is the applied bias at the electrode. The calculated carrier density of STO and R-STO are 9.5×10^{15} and 3.5×10^{17} cm^{-3} separately, which indicates that the reduction process induces an exponential increase of electron density in $SrTiO_3$, due to the introduction of substantial oxygen vacancies.

In fact, during aluminum reduction process, molten aluminum reductant loses electrons and Ti^{4+} ions accept electrons, while the appended oxygen ions transfer from TiO_2 to Al_2O_3 on the basis of the law of electron conservation. Consequently, the donor density and electrical conductivity of the black R-STO could be greatly enhanced. The expected large upward shift of the Fermi level caused by the increased electron density can lead to a significantly bending of the band edge, which facilitates charge separation at the interface of R-STO and electrolyte. Therefore, the improved charge transport and the facilitated charge separation resulted in the much more efficient photoelectrochemical water-splitting.

Conclusions

In summary, black $SrTiO_3$ nanocrystals with high photocatalytic activity have been successfully synthesized by alkaline hydrothermal method and subsequently reduced at moderate temperature by aluminum in a two-zone furnace. R-STO exhibits high stability under irradiation. A large amount of Ti^{3+} ions and oxygen vacancies are introduced into the reduced $SrTiO_3$, which enables significant enhanced visible and near-infrared light absorption and improved photocatalytic activity. The photocatalytic hydrogen generation of black $SrTiO_3$ is 2.5 times higher than that of pristine strontium titanate and show good cycling performance. The prepared black strontium titanate films also demonstrate a significant increase (2.4 times) in photocurrent density under illumination. The present study motivates us to treat other metallic oxides with blackening for enhanced solar absorption and for the development of highly active photocatalysts.

Experimental

Synthetic procedures. The pristine $SrTiO_3$ nanoparticles were prepared by an alkaline hydrothermal method. Typically, 0.43 g $Sr(Ac)_2{\cdot}H_2O$ was dispersed in 10 mL H_2O to achieve solution A, and 0.48 g $Ti(SO_4)_2$ was dissolved in 10 mL H_2O to gain solution B. Under vigorous stirring condition, solution B was added into solution A, and then 4.0 g KOH pellets were added to get a white suspension. The suspension was transferred to a 40 mL Teflon-lined autoclave, which was sealed and placed in an oven at 240 °C for 24 h. The product, as denoted as STO, was washed firstly with 0.1M HCl, repeatedly with deionized water and ethanol, and then dried in air. Black $SrTiO_3$ nanocrystals, as denoted as R-STO, were obtained from pristine $SrTiO_3$ by molten aluminum reduction in a two-zone furnace, which is described elsewhere.[16] The black referenced $SrTiO_3$ sample prepared by solid-state reaction was also reduced by aluminum at 500 °C, which was denoted as SSR-STO and R-SSR-STO respectively. In a typical solid-state reaction procedure, the mixture of $SrCO_3$ and TiO_2 with a molar ratio 1:1 was calcined at 1000 °C for 12 h.

STO and R-STO films are prepared by dip coating the $SrTiO_3$ slurry on a clean FTO glass substrate. To prepare precursor slurry, 0.5 g of as-prepared STO nanoparticles and 0.4 g of ethyl cellulose were suspended in 3.6 mL of terpilenol. For film deposition, the substrates were first degreased, thoroughly cleaned and dried before deposition. Then the substrates were dipped in the viscous precursor slurry and pulled out at a uniform pulling rate of 1 mm s^{-1}, and dried at 60 °C. This procedure was repeated three times to get 150-nm thick $SrTiO_3$ film on a FTO glass. The as-prepared films were first annealed at 500 °C for 2 h in air to obtain STO films, and further aluminum-reduced at 500 °C for another 2 h to achieve R-STO films.

Photocatalytic H_2 generation. 100 mg of sample loaded with 0.5 wt% Pt was added to an aqueous methanol solution (200 mL, 20%) in a closed gas circulation system. The UV light was obtained from a 300 W Xe lamp. Methanol was used as a sacrificial reagent and the anodic reaction generating O_2 from H_2O did not occur. The amount of generated H_2 was determined by gas chromatography.

Photoelectrochemical cell (PEC). To characterize the photoelectrochemical performance of the samples, a typical three-electrode system was utilized to conduct electrochemical

measurements with an electrochemical workstation (CHI660B, CH Instruments), in which the STO film or R-STO film on a FTO substrate, a Pt wire, and an Ag/AgCl electrode were used as the working, counter, and reference electrodes, respectively. 1.0M NaOH aqueous solution (pH = 13.6) was used as the supporting electrolyte to maintain the stability of films. A set of linear sweeps and transient photocurrent responses were recorded in dark and under illumination. A 150W Xe lamp was used as the light source to simulate the sunlight irradiation. The light intensity was measured by a calibrated Si photodiode. Mott-Scotty plots were derived from impedance-potential tests conducted at a frequency of 1 kHz in dark.

Sample characterizations. Field emission scanning electron microscopy (FESEM) images were taken on a JEOL JSM-6400F microscope. Transmission electron microscope (TEM) images and selected area electron diffraction (SAED) patterns were obtained with a FEI Tecnai G2 F20 transmission electron microscope operated at 200 kV. Absorption spectra were obtained by UV-Vis-NIR spectrometer (Hitachi U-4100). Solid-state XRD patterns were obtained with a BrukerD8 advance diffractometer operating with $Cu_{K\alpha}$ radiation. XPS experiments were carried out on a RBD upgraded PHI-5000C ESCA system (PerkinElmer) with $Mg_{K\alpha}$ radiation (hv = 1253.6 eV). PL spectra were measured at 300 K on a fluorescence spectrophotometer (F-4600, Hitachi, Japan) with an excitation wavelength of 320 nm.

Acknowledgements

This work is financially supported by NSF of China (Grant nos. 51125006, 91122034, 51272270, 61376056), and STC of Shanghai (Grant nos. 13JC1405700, 14520722000 and 14YF1406500). Shanghai Technical Platform for Testing and Characterization on Inorganic Materials (14DZ2292900).

Notes and references

[a] CAS Key Laboratory of Materials for Energy Conversion and State Key Laboratory of High Performance Ceramics and Superfine Microstructures, Shanghai Institute of Ceramics, Chinese Academy of Sciences (CAS), Shanghai 200050, P.R. China.

[b] Beijing National Laboratory for Molecular Sciences and State Key Laboratory of Rare Earth Materials Chemistry and Applications, College of Chemistry and Molecular Engineering, Peking University, Beijing 100871, P.R. China.

1 M. R. Hoffmann, S. T. Martin, W. Y. Choi and D. W. Bahnemann, *Chem Rev*, 1995, **95**, 69-96.

2 H. Tong, S. X. Ouyang, Y. P. Bi, N. Umezawa, M. Oshikiri and J. H. Ye, *Adv Mater*, 2012, **24**, 229-251.

3 X. Chen and S. S. Mao, *Chem Rev*, 2007, **107**, 2891-2959.

4 X. J. Lu, F. Q. Huang, X. L. Mou, Y. M. Wang and F. F. Xu, *Adv Mater*, 2010, **22**, 3719.

5 X. J. Lu, X. L. Mou, J. J. Wu, D. W. Zhang, L. L. Zhang, F. Q. Huang, F. F. Xu and S. M. Huang, *Adv Funct Mater*, 2010, **20**, 509-515.

6 W. J. Yin, H. W. Tang, S. H. Wei, M. M. Al-Jassim, J. Turner and Y. F. Yan, *Phys Rev B*, 2010, **82**.

7 R. Asahi, T. Morikawa, T. Ohwaki, K. Aoki and Y. Taga, *Science*, 2001, **293**, 269-271.

8 H. Irie, Y. Watanabe and K. Hashimoto, *Chem Lett*, 2003, **32**, 772-773.

9 G. M. Wang, H. Y. Wang, Y. C. Ling, Y. C. Tang, X. Y. Yang, R. C. Fitzmorris, C. C. Wang, J. Z. Zhang and Y. Li, *Nano Lett*, 2011, **11**, 3026-3033.

10 X. B. Chen, L. Liu, P. Y. Yu and S. S. Mao, *Science*, 2011, **331**, 746-750.

11 H. Pan, Y. W. Zhang, V. B. Shenoy and H. J. Gao, *J Phys Chem C*, 2011, **115**, 12224-12231.

12 C. H. Sun, Y. Jia, X. H. Yang, H. G. Yang, X. D. Yao, G. Q. Lu, A. Selloni and S. C. Smith, *J Phys Chem C*, 2011, **115**, 25590-25594.

13 X. H. Lu, G. M. Wang, T. Zhai, M. H. Yu, J. Y. Gan, Y. X. Tong and Y. Li, *Nano Lett*, 2012, **12**, 1690-1696.

14 Z. Wang, C. Y. Yang, T. Q. Lin, H. Yin, P. Chen, D. Y. Wan, F. F. Xu, F. Q. Huang, J. H. Lin, X. M. Xie and M. H. Jiang, *Adv Funct Mater*, 2013, **23**, 5444-5450.

15 D. Y. Wan, C. Y. Yang, T. Q. Lin, Y. F. Tang, M. Zhou, Y. J. Zhong, F. Q. Huang and J. H. Lin, *Acs Nano*, 2012, **6**, 9068-9078.

16 Z. Wang, C. Y. Yang, T. Q. Lin, H. Yin, P. Chen, D. Y. Wan, F. F. Xu, F. Q. Huang, J. H. Lin, X. M. Xie and M. H. Jiang, *Energ Environ Sci*, 2013, **6**, 3007-3014.

17 G. L. Zhu, T. Q. Lin, X. J. Lu, W. Zhao, C. Y. Yang, Z. Wang, H. Yin, Z. Q. Liu, F. Q. Huang and J. H. Lin, *J Mater Chem A*, 2013, **1**, 9650-9653.

18 H. Yin, T. Q. Lin, C. Y. Yang, Z. Wang, G. L. Zhu, T. Xu, X. M. Xie, F. Q. Huang and M. H. Jiang, *Chem-Eur J*, 2013, **19**, 13313-13316.

19 S. X. Ouyang, H. Tong, N. Umezawa, J. Y. Cao, P. Li, Y. P. Bi, Y. J. Zhang and J. H. Ye, *J Am Chem Soc*, 2012, **134**, 1974-1977.

20 A. E. Souza, G. T. A. Santos, B. C. Barra, W. D. Macedo, S. R. Teixeira, C. M. Santos, A. M. O. R. Senos, L. Amaral and E. Longo, *Cryst Growth Des*, 2012, **12**, 5671-5679.

21 Y. Qin, G. Y. Wang and Y. J. Wang, *Catal Commun*, 2007, **8**, 926-930.

22 D. A. Tenne, I. E. Gonenli, A. Soukiassian, D. G. Schlom, S. M. Nakhmanson, K. M. Rabe and X. X. Xi, *Phys Rev B*, 2007, **76**.

23 F. A. Rabuffetti, H. S. Kim, J. A. Enterkin, Y. M. Wang, C. H. Lanier, L. D. Marks, K. R. Poeppelmeier and P. C. Stair, *Chem Mater*, 2008, **20**, 5628-5635.

24 J. J. Liu and Q. F. Ge, *Chem Commun*, 2006, 1822-1824.

25 J. M. Coronado, A. J. Maira, J. C. Conesa, K. L. Yeung, V. Augugliaro and J. Soria, *Langmuir*, 2001, **17**, 5368-5374.

26 J. Pan, G. Liu, G. M. Lu and H. M. Cheng, *Angew Chem Int Edit*, 2011, **50**, 2133-2137.

27 M. G. Walter, E. L. Warren, J. R. McKone, S. W. Boettcher, Q. X. Mi, E. A. Santori and N. S. Lewis, Chem Rev, 2010, 110, 6446-6473.

28 K. L. Zhang, X. P. Lin, F. Q. Huang and W. D. Wang, *Journal of Molecular Catalysis a-Chemical* 2006, **258**, 185-190.

29 X. P. Lin, F. Q. Huang, W. D. Wang, Y. M. Wang, Y. J. Xia and J. L. Shi, *Applied Catalysis a-General* 2006, **313**, 218-223.

30 X. D. Jiang, Y. P. Zhang, J. Jiang, Y. S. Rong, Y. C. Wang, Y. C. Wu and C. X. Pan, *J. Phys. Chem. C*, **2012**, 116, 22619.

31 X. B. Chen, L. Liu and F. Q. Huang, *Chemical Society Reviews*, **2015**, 44, 1861-1885.
32 T. Xia, Y. H. Cao, N. A. Oyler, J. Murowchick, L. Liu and X. B. Chen, *Acs Applied Materials & Interfaces*, **2015**, 7, 10407-10413.
33 L. H. Tian, X. D. Yan, J. L. Xu, P. Wallenmeyer, J. Murowchick, L. Liu and X. B. Chen, *Journal of Materials Chemistry A*, **2015**, 3, 12550-12556.
34 T. Xia, P. Wallenmeyer, A. Anderson, J. Murowchick, L. Liu and X. B. Chen, *Rsc Advances*, **2014**, 4, 41654-41658.
35 T. Sun and M. Lu, *Applied Physics a-Materials Science & Processing*, **2012**, 108, 171-175.
36 H. Q. Tan, Z. Zhao, W. B. Zhu, E. N. Coker, B. S. Li, M. Zheng, W. X. Yu, H. Y. Fan and Z. C. Sun, *Acs Applied Materials & Interfaces*, **2014**, 6, 19184-19190.

Black $SrTiO_3$ nanocrystals with enhanced visible-light and even IR absorption have been successfully synthesized by aluminum reduction.